

A printability assessment framework for fabricating low variability nickel-niobium parts using laser powder bed fusion additive manufacturing

Bing Zhang

Wm Michael Barnes'64 Department of Industrial and Systems Engineering, Texas A&M University, College Station, Texas, USA

Raiyan Seede and Austin Whitt

Department of Materials Science and Engineering, Texas A&M University, College Station, Texas, USA

David Shoukr

Wm Michael Barnes'64 Department of Industrial and Systems Engineering, Texas A&M University, College Station, Texas, USA

Xueqin Huang, Ibrahim Karaman and Raymundo Arroyave

Department of Materials Science and Engineering, Texas A&M University, College Station, Texas, USA, and

Alaa Elwany

Wm Michael Barnes'64 Department of Industrial and Systems Engineering, Texas A&M University, College Station, Texas, USA

Abstract

Purpose – There is recent emphasis on designing new materials and alloys specifically for metal additive manufacturing (AM) processes, in contrast to AM of existing alloys that were developed for other traditional manufacturing methods involving considerably different physics. Process optimization to determine processing recipes for newly developed materials is expensive and time-consuming. The purpose of the current work is to use a systematic printability assessment framework developed by the co-authors to determine windows of processing parameters to print defect-free parts from a binary nickel-niobium alloy (NiNb5) using laser powder bed fusion (LPBF) metal AM.

Design/methodology/approach – The printability assessment framework integrates analytical thermal modeling, uncertainty quantification and experimental characterization to determine processing windows for NiNb5 in an accelerated fashion. Test coupons and mechanical test samples were fabricated on a ProX 200 commercial LPBF system. A series of density, microstructure and mechanical property characterization was conducted to validate the proposed framework.

Findings – Near fully-dense parts with more than 99% density were successfully printed using the proposed framework. Furthermore, the mechanical properties of as-printed parts showed low variability, good tensile strength of up to 662 MPa and tensile ductility 51% higher than what has been reported in the literature.

Originality/value – Although many literature studies investigate process optimization for metal AM, there is a lack of a systematic printability assessment framework to determine manufacturing process parameters for newly designed AM materials in an accelerated fashion. Moreover, the majority of existing process optimization approaches involve either time- and cost-intensive experimental campaigns or require the use of proprietary computational materials codes. Through the use of a readily accessible analytical thermal model coupled with statistical calibration and uncertainty quantification techniques, the proposed framework achieves both efficiency and accessibility to the user. Furthermore, this study demonstrates that following this framework results in printed parts with low degrees of variability in their mechanical properties.

Keywords Nickel-niobium Alloy, Laser powder bed fusion additive manufacturing, Printability maps, Statistical calibration, Density, Microstructure, Mechanical properties

Paper type Research paper

1. Introduction

Additive manufacturing (AM) is a well-established manufacturing technology capable of producing parts with complex geometries

and intricate features, among many other benefits it offers (Cotteleer and Joyce, 2014; Ngo *et al.*, 2018). To unlock AM's full potential, however, more developments are yet to be conducted

The current issue and full text archive of this journal is available on Emerald Insight at: <https://www.emerald.com/insight/1355-2546.htm>

The authors acknowledge the funding support from the Army Research Office (ARO) under Contract No. W911NF-18-1-0278 and the National Science Foundation (NSF) under grant number CMMI-1846676. RA and XH also acknowledge Lawrence Livermore National Laboratory under contract No. B641173, *Collaborative Research and Development for LLNL Missions* program.



Rapid Prototyping Journal
© Emerald Publishing Limited [ISSN 1355-2546]
[DOI 10.1108/RPJ-01-2021-0024]

Received 30 January 2021

Revised 6 May 2021

Accepted 9 June 2021

especially in the areas of materials design and process optimization to enable successful printing of defect-free parts and reduce variability in the properties of fabricated parts (Fayazfar et al., 2018; Ar isoy et al., 2017; Song et al., 2012).

Determining processing recipes for newly designed AM materials can be time- and cost-intensive before a successful print (i.e. a part with near-full density and the minimal amount of macroscopic defects) is realized. One approach reported in the literature is through parameter sweeps or Taguchi-based design of experiments, which require printing sufficiently large numbers of samples under different experimental settings (Hanzl et al., 2015; Mingear et al., 2019). Another approach that aims to reduce the number of experiments is to use optimized processing parameters that have been previously established for a material with comparable elemental composition. However, the similarity in elemental constituents does not necessarily guarantee that the same optimized processing parameters would result in successful prints. For example, a nickel-niobium alloy (NiNb₅, 5.08 Wt.% of Nb) has been recently used as a binary approximation for Inconel 718 (Karayagiz et al., 2020). The optimized processing parameters of Inconel 718 did not work for printing NiNb₅. This is due to the effect of other constituent elements (e.g. Cr, Fe, Mo, Al) in Inconel 718, which affect physical properties of the material and, in turn, influence quality of as-printed parts.

In contrast to the above experimental-based approaches, other efforts have followed a modeling-based approach to save experimental costs. Both finite element models and analytical models have been applied to simulate the complex melting-solidification processes involved in metal AM (Schoinochoritis et al., 2017; Krol et al., 2013). Robust design has also been applied to account for unknown thermo-physical material properties through modeling them as noise factors into the simulation model (Wang et al., 2019). Although these model-based approaches can potentially save some experimental burden, in reality these simulation models exhibit uncertainty that need to be first accounted for to ensure their predictions agree are representative of the manufacturing process (Hu and Mahadevan, 2017). Moreover, the majority of these models are not readily accessible for all AM practitioners. Needless to say, they are typically computationally expensive which limits their practicality for process planning and optimization.

Some recent studies in the literature indicate that AM process parameters can be determined via single-track experiments and/or melt pool modeling approach. Bosio et al. developed laser power-scan speed processing maps using single-track experiments for the laser powder bed fusion (LPBF) process (Bosio et al., 2019). A simplified analytical melt pool model and single-track samples of the LPBF process are used to create a novel density control algorithm (Letenneur et al., 2019). In that paper, an energy density-build rate processing map is numerically generated and experimentally calibrated to support the optimization of printed samples' density.

The current work aims to utilize a systematic framework developed by the co-authors in previous work (Seede et al., 2020) to determine processing windows for a binary nickel-niobium alloy NiNb₅ using LPBF metal AM processes. The processing windows will enable the fabrication of as-printed parts free of porosity due to the following:

- lack of fusion (LOF);
- keyholing; and
- balling.

An underlying hypothesis is that through the fabrication of as-printed parts with more than 99% density, good quality parts with low degrees of variability in mechanical properties and consistent microstructures can be achieved, as will be demonstrated in the validation case study. The processing windows obtained using the proposed framework will be referred to as *printability maps* in the remainder of the paper. A printability map essentially divides the processing parameters space defined by laser power "*P*", laser scan speed "*V*", and hatch spacing "*h*" into regions indicating the outcome of printing a part using different combinations of these parameters. An example of a printability map is depicted in Figure 1.

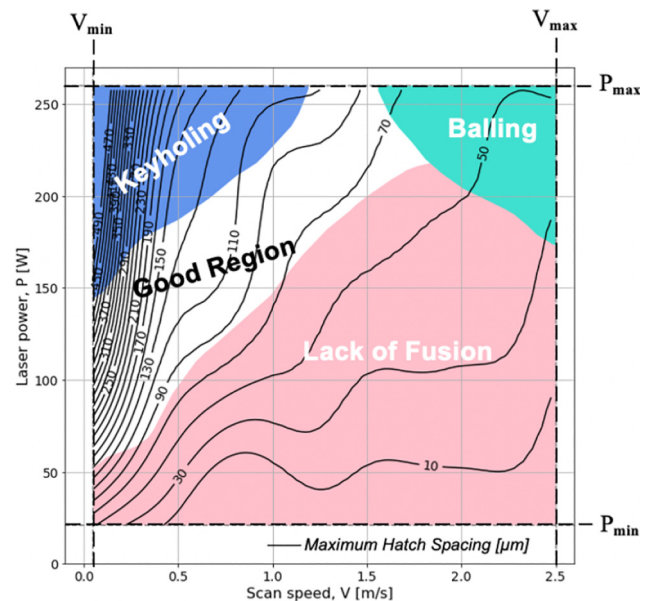
The systematic framework proposed to construct printability maps is described in Section 2. Microstructural and mechanical properties characterization of printed samples guided by the printability map are reported in Section 3. The paper is concluded with discussion and insights in Section 4.

2. Printability map development for NiNb₅

2.1 Nickel-niobium alloy (NiNb₅)

To simplify the modeling of Nb segregation during rapid solidification of Ni-based alloys, a newly developed binary NiNb₅ alloy has been proposed as a surrogate in previous works (Karayagiz et al., 2020; Johnson et al., 2019). In the current study, gas atomized NiNb₅ powder produced by Nanoval GmbH & Co. KG is used. The exact composition of the powder was determined using inductively coupled plasma atomic emission spectroscopy (ICP-AES) with 5.08 (± 0.91) Wt.% of Nb and the remaining being Ni. NiNb₅ powder particles were characterized using a scanning electron

Figure 1 An example of a printability map for a generic alloy with different regions corresponding to outcomes of the printing process



Note: The contour lines represent maximum hatch spacing

microscope (SEM), as shown in Figure 2. The particle size distribution and density of the alloy were determined by the supplier, reporting that 80% of the powder particles are smaller than or equal to $30\ \mu\text{m}$ ($d_{80} = 30\ \mu\text{m}$) and that the bulk density " ρ " of the material is $8909\ \text{kg}/\text{m}^3$ (at room temperature). The melting temperature of this alloy is $T_m = 1703\ \text{K}$.

Other unknown material properties were estimated as follows: thermal conductivity " k ", specific heat capacity " c " and boiling temperature " T_b " were approximated using the rule of mixture for Ni and Nb, and computed as $70.4\ \text{W}/(\text{m} \cdot \text{K})$, $636.19\ \text{J}/(\text{kg} \cdot \text{K})$, $3103\ \text{K}$, respectively (Chase, 1996; Valencia and Queded, 2013; 2021; Zhang et al., 2011). These properties were selected at the melting temperature in the solid-state as an approximate reference point. The absorptivity " A " of the material was approximated using the calculated value for a Gaussian distributed laser beam with $1\ \mu\text{m}$ wavelength melting of Ni powder which has an average powder particle radius of $13.5\ \mu\text{m}$ and the value is 0.51 (Boley et al., 2016).

2.2 Analytical thermal model

The first step in constructing a printability map is through establishing a relationship between AM process parameters and melt pool geometry. This can then be used to define sub-regions within the process parameters space that correspond to different modes of printing (LOF, keyholing, balling and good prints). To generate such a map, a full sweep within the parameters space must first be performed. To achieve this in a practical fashion, a relatively low fidelity analytical model developed by T. W. Eagar and N. S. Tsai (E-T) is used to simulate melt pool geometry across the " $P - V$ " parameter space (Eagar and Tsai, 1983). Although the model is known to have simplifying assumptions that exclude some physics related to convection and keyhole modes, it represents a reasonable approximation for a starting step. Furthermore, an integral part of our systematic framework involves subsequent statistical calibration to adjust the model predictions such that they agree with experimental observations as described later in section 2.5 (Kasperovich et al., 2016).

The input parameters of the E-T model include NiNb_5 thermo-physical material properties stated in section 2.1, process parameters (in particular, laser power and scan speed) and laser beam size. The laser beam size of the commercial LPBF AM system used in the current study (ProX200 DMP by

3D Systems) is $80\ \mu\text{m}$ in diameter. E-T model simulations are used to define sub-regions in the printability map according to defect criteria that are discussed in the next section.

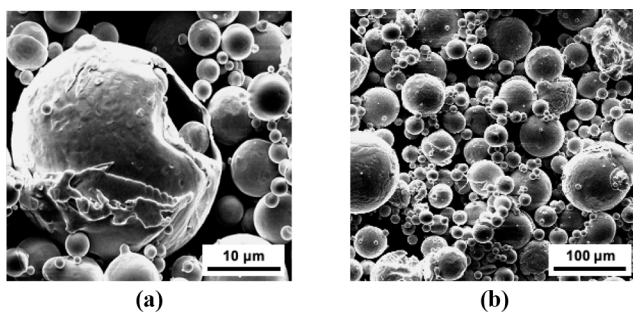
2.3 Criteria for establishing the printable region

Using the E-T analytical thermal model, the melt pool width and depth can be simulated for any processing parameter combinations. Our first goal is to reduce the parameter space from a theoretically infinite space in the positive quadrant to a finite space. As a first step, upper and lower bounds for the laser power and scan speed, respectively, are established. The upper bound on the scan speed, " V_{max} ", is set to the maximum attainable speed by the laser optics on the AM system while the lower bound, " V_{min} ", is set to an arbitrarily small value slightly above the theoretical minimum (i.e. zero). Because the E-T model requires a moving heat source, $0.05\ \text{m}/\text{s}$ is taken as the lower bound on the laser speed. The upper bound on the laser power, " P_{max} ", is set as the maximum power attainable by the AM system (i.e. a machine limitation). The lower bound on the laser power, " P_{min} ", is set as the minimum laser power needed to cause melting at a speed of " V_{min} ". This value can be computed using the E-T model. The bounds were determined as $P_{min} = 65\ \text{W}$, $P_{max} = 260\ \text{W}$, $V_{min} = 0.05\ \text{m}/\text{s}$ and $V_{max} = 2.5\ \text{m}/\text{s}$.

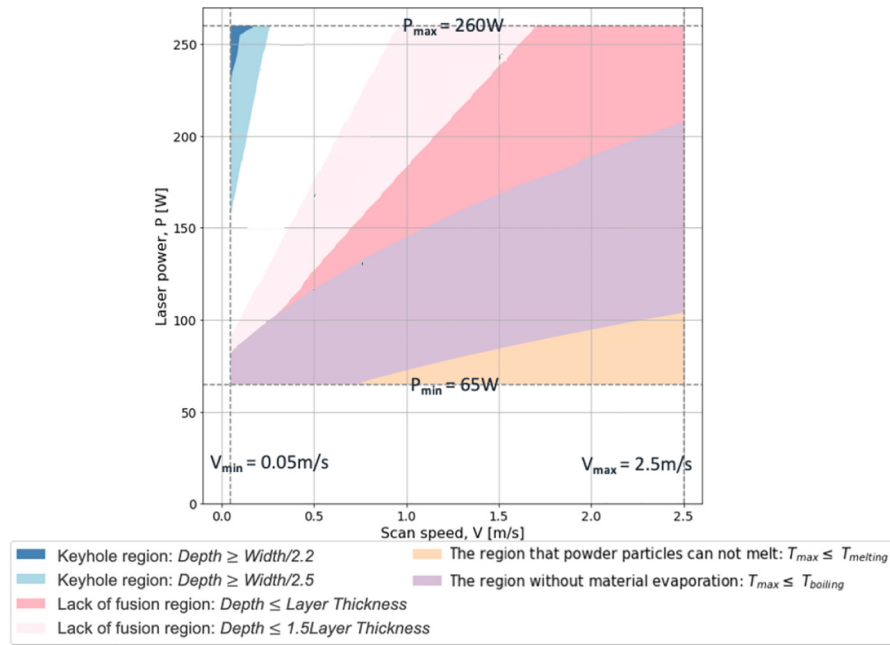
Next, the E-T model is used to further split this space into sub-regions corresponding to different printing modes that could result in porosity; namely, LOF, keyholing and balling, as depicted in Figure 3. LOF porosity is due to voids that create among unmelted or incompletely melted powder particles. Theoretically, LOF occurs when melt pool depth is smaller than powder layer thickness, $\frac{D}{t} < 1$. To be more conservative, the threshold of $\frac{D}{t} < 1.5$ is also considered for our study. Keyhole porosity occurs when the deposited laser power is sufficient to cause evaporation of the metal and formation of plasma which leads to the development of a vapor cavity. This enables the laser beam to "drill" to a far deeper depth forming a key shape than is possible in general conduction mode. Literature reported that keyhole mode can be characterized by an aspect ratio of $\frac{W}{D}$ which is material dependent (King et al., 2014). Here, two thresholds for determining keyholing $\frac{W}{D} < 2.5$ and $\frac{W}{D} < 2.2$ are considered. Balling is a phenomenon where the molten track shrinks and breaks into a row of discontinuous segments to reduce the surface energy by the surface tension if the molten material does not wet the underlying substrate (Brandt, 2016). Balling is likely to happen when the melting-solidification process takes place under low energy density and very fast scan speed (Zhou et al., 2015; Yadroitsev et al., 2013). In order to classify the balling sub-region, a support vector machine (SVM) machine learning algorithm is used to fit the characterized balling singles based on their morphology. This will be discussed in section 2.6 and later updated in the revised printability map.

In addition to the above three modes, two more thermal-based criteria are considered in the initial printability map as displayed in Figure 3: lack of melting and evaporation. E-T simulations for NiNb_5 with parameter combinations resulting in a maximum melt pool temperature T_{max} less than $T_m = 1703\ \text{K}$ means that these combinations' energy is too low to melt any of the powder particles. By plotting another boundary with T_{max} equal to the boiling temperature $T_b = 3103\ \text{K}$, a new sub-region is formed within the finite space.

Figure 2 SEM micrographs of NiNb_5 powder particles



Notes: (a) A high magnification image showing the surface morphology of powder particles; (b) a low magnification image showing the powder size distribution

Figure 3 Initial printability map for NiNb₅ generated using the E-T model and defect criteria

This means that material evaporation occurs above this sub-region. These two criteria are only included in the initial printability map as guidance of the design of experiments. For example, few single tracks need to be conducted within the lack of melting sub-region.

2.4 Single track experiments

The objective of single-track experiments is twofold:

1. to revise E-T model predictions and ensure they are agreement with experimental observations; and
2. to validate the relationship between melt pool dimensions and LOF, keyholing and balling formation mechanisms.

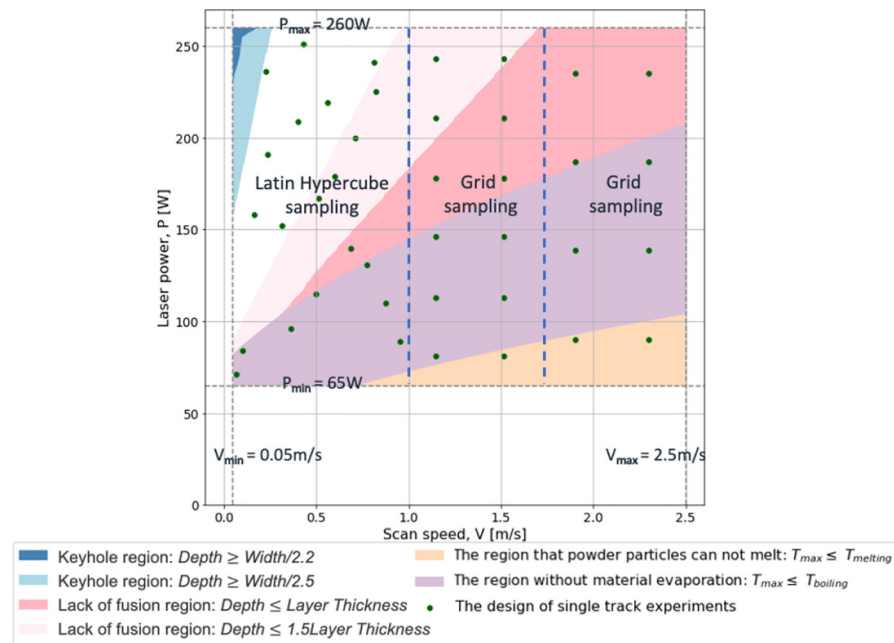
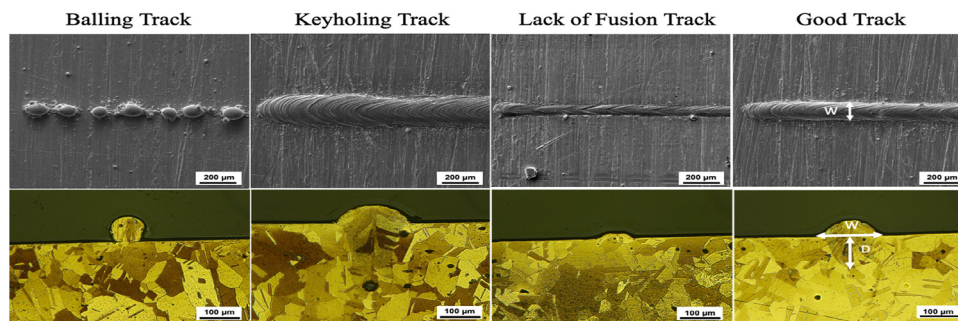
Recall that the E-T exhibits both parameter and model uncertainties (for example, uncertainty in the thermo-physical material parameters used as input to the model). Before finalizing the printability map, it is important to ensure that these uncertainties are quantified and accounted for such that model predictions of melt pool width and depth are in agreement with experimental characterization. This is a process formally known as statistical calibration which will be described in the Section 2.5. Single-track experiments were conducted to obtain experimental data needed for calibration. To initialize the experiment, 40 processing parameter combinations were selected based on the initial printability map. Both Latin hypercube sampling (LHS) and grid sampling methods were used to design the experiments, as shown in Figure 4. LHS was implemented in the region ending with the $\frac{D}{l} = 1.5$, criterion which is the main area of interest. In that area, as many processing parameter combinations as possible are sampled randomly and uniformly. Using LHS, no two design points (or parameter combinations) share the same values for any parameter. Grid sampling – the simplest experimental design method – was applied to the other two areas with different levels of sparsity split by the ending point of another LOF criteria $\frac{D}{l} = 1$, as depicted in Figure 4.

In conducting single-track experiments, a NiNb₅ 70 mm × 40 mm × 3 mm dimension stage was first printed using 200 W laser power, 1 m/s scan speed and 120 μm hatch spacing. This stage was normalized under argon at 1100 °C for 1 h and air-cooled. Next, forty 10 mm long single tracks were printed 1 mm apart from each other on the stage covered by a layer of powder. The layer thickness was set to d_{80} which is 30 μm . Three cross-sections were cut from each track using wire electrical discharging machining (wire EDM). Then the specimens were polished down to 0.25 μm , then vibratory polished in colloidal silica. Kalling's solution No.2 (5 g CuCl₂, 100 mL HC₁ and 100 mL ethanol) was used to etch the single tracks. Figure 5 depicts representative track top views and cross sections from single-track experiments. Melt pool width and depth of each polished and etched cross-section was measured three times using optical microscopy (OM) software. Averages of these nine measurements were taken as the experimental results.

2.5 Statistical calibration of the E-T thermal model

We follow a two-step multivariate Bayesian calibration framework proposed by Mahmoudi and Tapia in (Mahmoudi et al., 2018; Kennedy and O'Hagan, 2001; Campbell, 2006). The interested reader should refer to his previous work for details regarding the Bayesian procedure. Here, we mainly discuss how to apply this calibration framework to calibrate the E-T model for NiNb₅.

Three thermo-physical material properties were identified as calibration parameters: thermal conductivity “ k ”, specific heat capacity “ c ” and absorptivity “ A ”. A large sampling range of these parameters was selected to ensure calibration accuracy (the degree of agreement of the calibrated model predictions with experimental observations). The sampling ranges of “ k , c , A ” are [10, 100], [450, 650], (0,1), respectively. The prior distribution for each parameter was taken as a non-informative Uniform distribution defined by these values for the support of

Figure 4 The initial printability map of NiNb₅ with 40 selected process parameter combinations for single track experiments**Figure 5** Representative SEM images of as-printed track top views (top row) and OM images of etched melt pool cross sections (bottom row) for a balling track, a keyholing track, a LOF track, and a good track

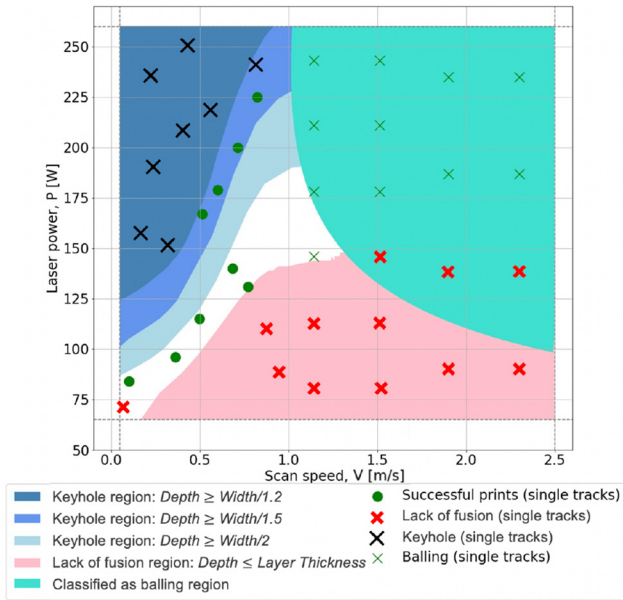
the distribution. Bayesian calibration was then conducted to revise these prior distributions using a small number of experimental data and determine the posterior distributions of calibration parameters. The mode of each posterior distribution (the value that corresponds to the highest probability density function) was then used as the estimated value of each calibration parameters. These were equal to $42.03 \text{ W}/(\text{m} * \text{K})$, $457.89 \text{ J}/(\text{kg} * \text{K})$ and 0.77 for “ k , c , A ”, respectively. Two more important outcomes of the calibration process are the discrepancy function that accounts and corrects for model bias and uncertainty and an error term that accounts for uncertainty in experimental measurements. Finally, the accuracy of the calibrated E-T model is determined through conducting 8-fold cross-validation to compute the mean average error (MAE) of melt pool width and depth predictions: $1.37 \mu\text{m}$ and $1.53 \mu\text{m}$. These correspond to mean absolute percentage errors (MAPE) of 1.6% and 4.05% for melt pool width and depth, respectively. The low MAPE values ($\leq 5\%$ error) indicate that the calibrated model yields very reasonable

predictions of melt pool geometry and now be used to revise and update the initial printability map.

2.6 Finalizing the printability map

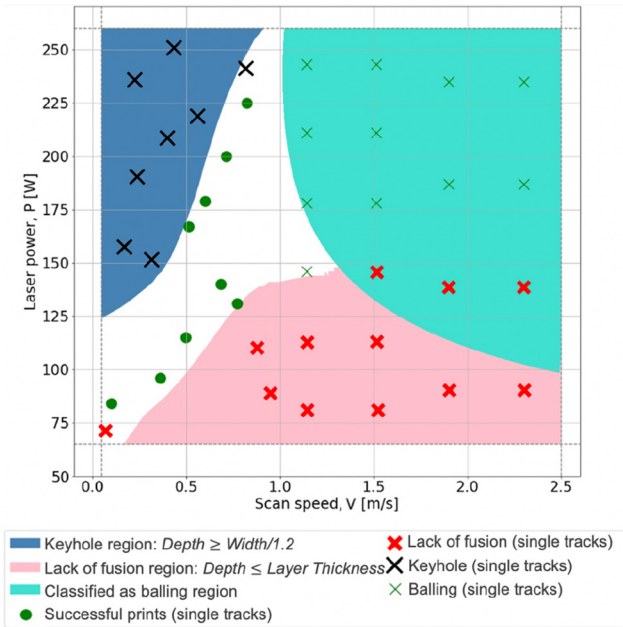
The revised printability map generated using the calibrated E-T model is depicted in Figure 6. Multiple keyholing regions were plotted on this map with different melt pool width-to-depth ratios. Forty experimental single tracks were overlaid on the map according to the experimentally observed melt pool morphology (from top-view and cross-sectional imaging). These can now be used to select the correct keyholing ratio for this specific NiNb₅ alloy. The keyholing criterion ratio $\frac{W}{D} < 1.2$ provides the best fit for classifying keyholing single tracks, only misclassifying 1 track, in contrast to $\frac{W}{D} < 1.5$ and $\frac{W}{D} < 2$ each of which misclassified 4 single tracks as having undergone keyholing. Thus, the keyholing region was finalized as the $\frac{W}{D} < 1.2$ criterion ratio, as shown in Figure 7. The boundary for the balling region was determined using an SVM classifier with

Figure 6 Revised printability map for NiNb₅ with experimental single tracks overlaid onto the map for validation



Note: Three different keyholing ratio criteria are displayed on this map

Figure 7 Revised printability map for NiNb₅ with the finalized criteria for each defect



a 3rd degree polynomial kernel applied to the single tracks that labeled as balled tracks. In the revised printability map, the SVM-classified balling region is overlapped with the LOF region. Only a tiny fraction of the tracks are misclassified or exist in both the balling and LOF defect regions.

The revised printability map in Figure 7 is limited to $P - V$ combinations, which are sufficient to print single tracks. To

print coupons (and ultimately parts), one needs to determine the hatch spacing parameter “ h ”, which is defined as the distance between two adjacent passes of the laser beam within the same layer. An approach for computing the maximum allowable hatch spacing is proposed by the co-authors in Seede et al (Eagar and Tsai 1983). This hatch spacing criterion is geometrically derived to promote full fusion for a given melt pool width “ W ”, melt pool depth “ D ” and layer thickness “ t ”. The maximum hatch spacing “ h_{max} ” for all processing parameter combinations in the printability map can be computed using the following equation, where melt pool width, W , and depth, D , can be computed using the calibrated E-T model predictions and t represents the layer thickness:

$$h_{max} = W \sqrt{1 - \frac{t \times D}{D(t + D)}}$$

Figure 8 shows the finalized printability map with maximum hatch spacing contours. In this case study, the computed maximum hatch distance was rounded down to the nearest multiple of five for each processing parameter combination when printing density coupons and mechanical test samples.

2.7 Fabricating density coupons and mechanical test blocks

Upon finalizing the printability map, the last step is to print density coupons and mechanical test blocks to validate it. The parts were printed on a pure Ni substrate. The scanning strategy used was bidirectional as depicted in Figure 9. The laser beam starts melting from the top corner and moves to the bottom corner at an angle of 45° with a 90° rotation between successive layers. All parts were printed at a constant layer thickness 30 μm similar to single-track experiments.

Figure 8 The finalized printability map of NiNb₅ generated using $\frac{W}{D} < 1.2$ keyholing criterion, $\frac{D}{t} < 1$ LOF criterion and SVM classifier for balling

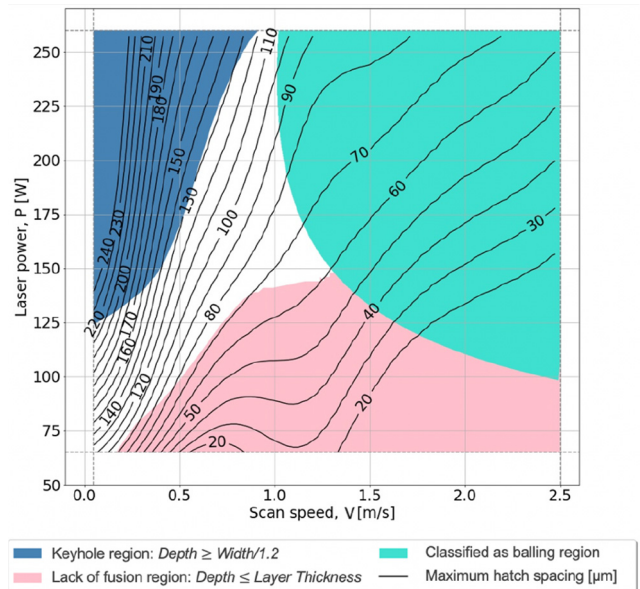
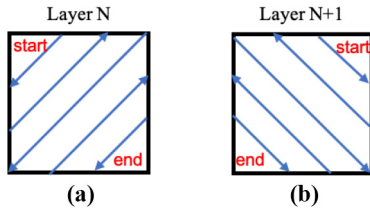
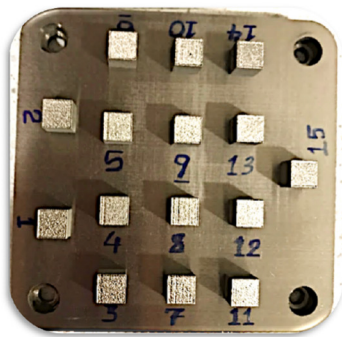
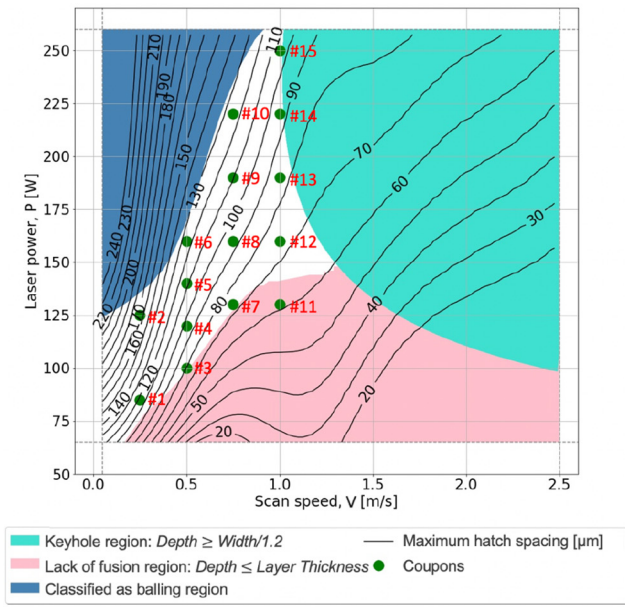


Figure 9 Laser scanning strategy for (a) layer N (b) successive layer N + 1



First, fifteen 10 mm × 10 mm × 10 mm coupons were printed using processing parameter combinations from within and around the good printability region as illustrated in Figure 10. The coupons were cut off from the substrate using wire EDM for density (or porosity) analysis. Three vertical cross-sections (with respect to the building direction) from the bottom, middle and top of each coupon were sliced, polished and etched using the same strategy as single tracks for microstructure evaluation. Compression samples

Figure 10 (a) Fifteen selected processing parameter combinations for printing density coupons are shown as green dots in the finalized printability map; (b) The as-printed fifteen coupons



with dimensions 8 mm × 4 mm × 4 mm were also cut from the coupons in both horizontal and vertical orientations (with respect to the building direction) using wire EDM.

Next, five processing parameter combinations were selected from the near full density coupons (coupons 3, 7, 8, 13 and 15 as shown in the next sub-section) to print mechanical test blocks marked in Figure 11(a). Five 10 mm × 10 mm × 34 mm blocks were first printed in horizontal orientation (with respect to the building direction) as depicted in Figure 11(b). Three 1 mm thick flat tensile samples were then cut with 26 mm overall length, 7 mm overall width, 8 mm gauge length and 3 mm gauge width from each block by wire EDM, as shown in Figure 12.

Room temperature monotonic loading tests for compression and tensile samples were conducted with an MTS 810 servo-hydraulic test frame at a strain rate of $5 \times 10^{-4} \text{ (s}^{-1}\text{)}$. And an extensometer with ceramic extension rods indirect contact with the gauge section of the samples recording axial strain. Grips equipped with WC platens were used to load and unload the samples.

Figure 11 (a) Five selected processing parameter combinations for printing mechanical test blocks are marked by red circles; and (b) The as-printed blocks from which tensile samples are cut

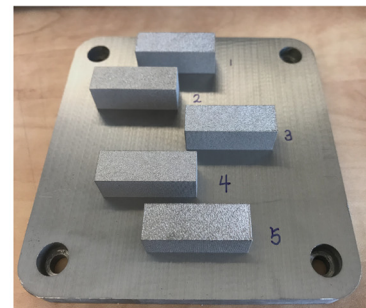
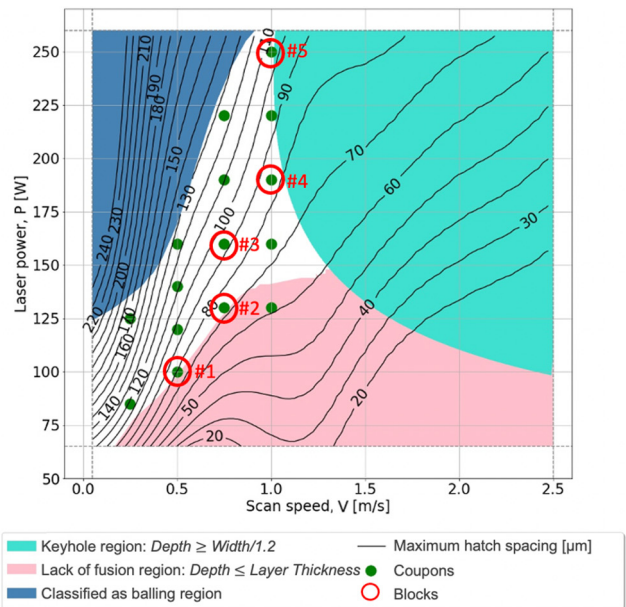
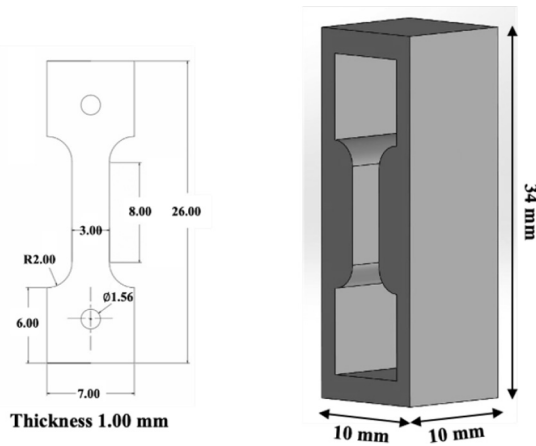


Figure 12 The schematic of the block and the mechanical test sample cut from it



3. Results and discussion

3.1 Density Analysis

Two different density measurement techniques were used to test the as-printed coupons (Spierings *et al.*, 2011): the common repeatable and non-destructive Archimedes method according to the ASTM B962-15 (A. S. for Testing, 2009) and microscopy analysis to gain further insight into the shape, size and distribution of the pores. Archimedes measurements were performed in ethanol with the density of each sample being measured one time. For the latter, three optical micrographs (OM) from vertical cross-sections of each coupon (with respect to the building direction) were taken for area percent porosity measurements. These OM images were processed by the software ImageJ® in order to calculate the area percentage of porosity in each image (ImageJ, 2012). The averaged measurements of each coupon from the Archimedes and OM methods are listed in Table 1.

Overall, the Archimedes density results are consistent with OM density results. However, the Archimedes density of coupons 7, 13 and 15 surpasses 100%. This is likely due to inaccuracy in bulk density of NiNb₅ estimate by the material supplier. On the other hand, the entire Archimedes density measurement process is manually operated, inevitably there will be operator errors. Due to these issues, OM density results were used for subsequent analysis. Figure 13 shows OM images of the polished coupon cross-sections displaying the porosity measurements for the fifteen coupons. It can be seen that 14 out of the 15 coupons have OM density above 99%, including coupon 11 that was selected close to the LOF region. Pores are visible along the adjacent tracks of coupons 2 and 10 with relatively lower OM density 94.45% and 99.03%. This is likely attributed to the proximity of the processing parameter combinations to the keyholing region and possibly due to large melt pool geometry prediction error in that $P - V$ area (as the equation for computing the maximum hatch spacing depends

Figure 13 OM images of the polished cross-sections for the fifteen coupons displaying porosity measurements

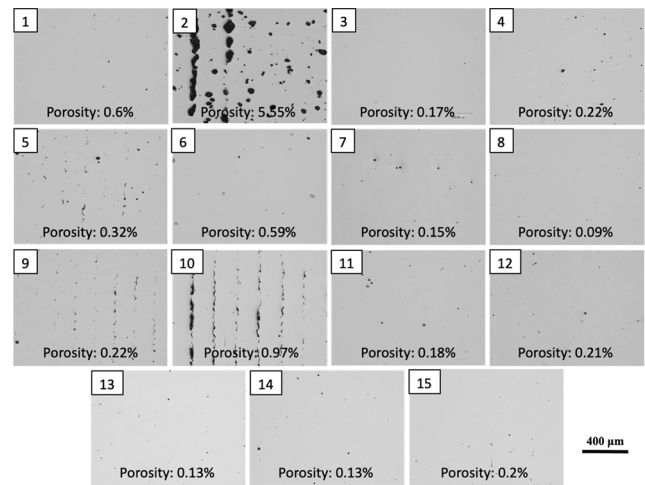


Table 1 Processing parameter combinations and corresponding density measurement results for NiNb₅ coupons

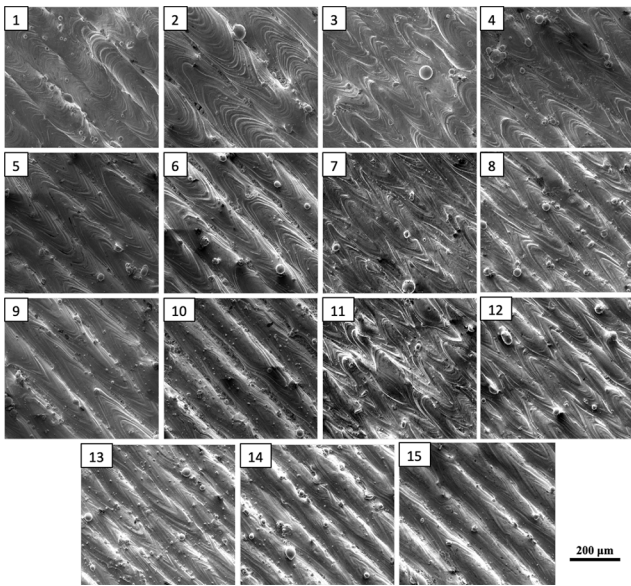
Coupon #	Laser Power (W)	Scan Speed (m/s)	Hatch Spacing (μm)	Layer Thickness (μm)	Linear Energy Density (J/m)	Archimedes Density (%)	OM Density (%)
1	85	0.25	100	30	340	99.79	99.40 \pm 0.33
2	125	0.25	165	30	500	96.58	94.45 \pm 1.42
3	100	0.5	70	30	200	99.73	99.83 \pm 0.11
4	120	0.5	95	30	240	99.59	99.78 \pm 0.03
5	140	0.5	110	30	280	99.63	99.68 \pm 0.14
6	160	0.5	125	30	320	99.14	99.42 \pm 0.22
7	130	0.75	65	30	173	100.11	99.85 \pm 0.05
8	160	0.75	90	30	213	99.98	99.91 \pm 0.08
9	190	0.75	110	30	253	99.87	99.78 \pm 0.15
10	220	0.75	125	30	293	99.95	99.03 \pm 0.75
11	130	1.0	55	30	130	99.87	99.82 \pm 0.04
12	160	1.0	70	30	160	99.67	99.79 \pm 0.04
13	190	1.0	80	30	190	100.51	99.84 \pm 0.06
14	220	1.0	95	30	220	99.95	99.87 \pm 0.05
15	250	1.0	105	30	250	100.08	99.80 \pm 0.11

on accurate melt pool dimensions). Lack of calibration of experimental data can lead to larger prediction errors for $P-V$ combinations. Prediction errors can result in larger hatch spacing parameter values being used for printing, resulting in porosity formation in as-printed coupons.

3.2 Microstructure Analysis

Figure 14 shows SEM micrographs of the NiNb₅ coupons' top surfaces. All fifteen coupons exhibit flat surfaces with

Figure 14 SEM micrographs of top surfaces for coupons 1–15



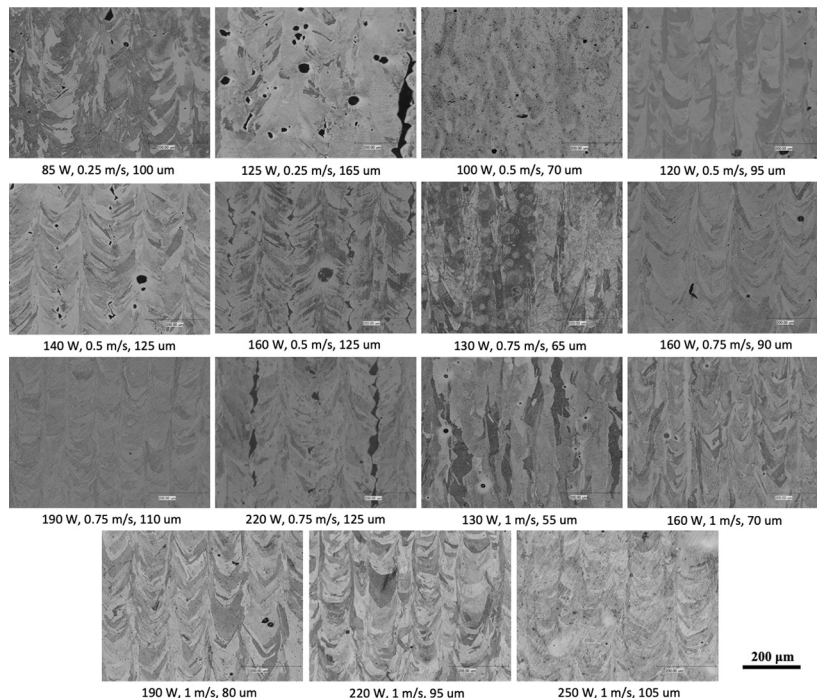
reasonably low roughness. As shown in the figure, Coupon 2 has gaps between tracks with powder particles inside which agrees with the OM density result. Indeed, 10 measurements of track widths were taken from the top surface for Coupon 2 and resulted in an average track width of $149.83 \mu m$, which is considerably smaller than its maximum hatch spacing parameter $165 \mu m$. For Coupon 11, it is difficult to distinguish the tracks at the top surface. This indicates low deposited energy within (as indicated by the linear energy density for Coupon 11 in Table 1).

Figure 15 shows the optical micrographs of each polished and etched vertical cross-section (with respect to the building direction) displaying the grain structure. Long and thin columnar grains are dominated with mixed small equiaxed grains in the as-printed coupons. The grain size of each coupon was calculated by taking the average of six measurements at the bottom, middle and top vertical cross-sections using the intercept method. Due to the relatively high cooling rates at the bottom of the vertical cross-section, grains are stretched towards the cooling direction. The average grain size is larger at the bottom of the vertical section than at the middle which is close to the top. For example, coupon 4 has the average grain size $42 \mu m$, $31 \mu m$ and $29 \mu m$ at the bottom, middle and top section, respectively. We also observe a larger grain size at higher scan speed when laser power is the same. For example, coupons 6, 8 and 12 with the same laser power and increasing scan speed, having an increasing grain size $26 \mu m$, $32 \mu m$ and $35 \mu m$.

3.3 Mechanical Properties

The fifteen horizontal and vertical compression samples (with respect to the building direction) as described in Section 2.7 were loaded and unloaded at around 14% strain before failure. The testing results are listed in Table 2 and the strain-stress curves are

Figure 15 OM images of each polished and etched NiNb₅ coupon vertical cross-section displaying the grain structure



plotted in Figure 16. There is a minor variance in the yield stress of these 15 coupons from same building direction. The difference between testing results in the horizontal and vertical samples is due to the microstructure and porosity difference.

Tensile testing was performed at room temperature through loading and unloading until failure. Three tensile samples were tested in each block and the average mechanical property values are listed in Table 3. Except for a higher average ultimate tensile strength (UTS) of 654 MPa and a greater average tensile ductility of 24% elongation

observed in the samples than the LPBF fabricated pure Ni (Yap *et al.*, 2021), the test results indicate low variability in these properties across different mechanical test blocks and similar ductility level to additively manufactured Inconel 718. By utilizing the printability framework, 51% larger tensile ductility than the result of the LPBF processed NiNb₅ reported in the literature (Atli *et al.*, 2021) was obtained. Figure 17 shows the almost same strain-stress relationships recorded under deformation of all tensile samples.

Table 2 Compression testing results of horizontal and vertical samples for NiNb₅ coupons

Coupon #	Horizontal Compression Sample			Vertical Compression Sample		
	Elastic Modulus (Mpa)	Yield Stress (MPa)	Yield Strain (%)	Elastic Modulus (Mpa)	Yield Stress (MPa)	Yield Strain (%)
1	86590.14	573.88	0.86	73344.69	544.24	0.97
2	79971.41	463.89	0.78	72063.43	520.34	0.92
3	86519.50	584.95	0.88	85954.67	567.12	0.86
4	116365.94	628.12	0.74	119016.62	593.92	0.70
5	119456.90	614.40	0.71	120739.98	576.05	0.68
6	100731.86	583.53	0.78	109265.36	553.97	0.71
7	114987.34	616.22	0.74	125612.73	559.33	0.65
8	125954.77	625.90	0.70	124153.98	560.76	0.65
9	118828.53	604.32	0.71	90860.96	582.54	0.84
10	118697.41	582.00	0.69	94658.33	573.37	0.81
11	125194.34	604.98	0.68	101140.89	525.65	0.72
12	129512.16	628.68	0.69	118604.22	561.88	0.67
13	129116.18	612.02	0.67	117183.81	583.69	0.68
14	107177.32	608.22	0.77	99875.00	564.70	0.77
15	97895.69	622.53	0.84	98247.88	569.28	0.78

Figure 16 (a) Compression testing results of 15 coupons tested in the horizontal direction. (b) Compression testing results of 15 coupons tested in the vertical direction

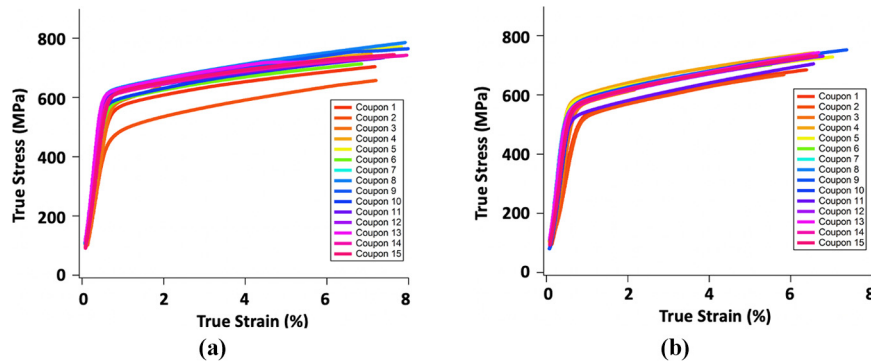
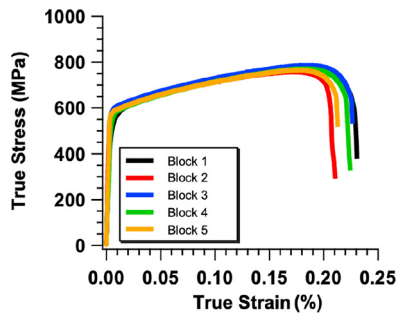


Table 3 Mechanical properties from tensile testing of as-printed NiNb₅

Block #	Laser Power (W)	Scan Speed (m/s)	Hatch Spacing (μm)	Layer Thickness (μm)	Ultimate Tensile Strength (MPa)	Elongation (%)
1	100	0.5	70	30	652.2 \pm 4.0	24.8 \pm 1.0
2	130	0.75	65	30	646.8 \pm 2.6	22.8 \pm 0.6
3	160	0.75	90	30	662.4 \pm 3.2	24.9 \pm 0.5
4	190	1.0	80	30	656.7 \pm 2.7	25.4 \pm 0.2
5	250	1.0	100	30	652.6 \pm 1.6	22.7 \pm 1.0

Figure 17 Strain–stress curves for the five mechanical test blocks

Mechanical testing results indicate that through adequately avoiding LOF, keyholing and balling (guided by the printability map) to print near-full density coupons and samples, variations in P , V and h do not have significant influence on the mechanical properties. By employing the proposed printability framework, NiNb₅ parts with good quality and repeatability were successfully produced.

4. Conclusion

This study reports the fabrication of defect-free NiNb₅ parts using LPBF AM with excellent mechanical properties and low degrees of variability through following a systematic printability assessment framework. The framework integrates analytical thermal modeling, uncertainty quantification and experimental characterization to determine processing windows for printing near-full density parts through mitigating LOF, balling and keyholing defects.

Through utilizing this printability framework, 99.3% of as-printed coupons guided by the printability map achieved >99% density (with some coupons achieving up to 99.9% density). Mechanical testing of samples fabricated using the five process parameter combinations with highest density resulted in good mechanical properties with very low degrees of variability. Tensile strains 20% larger than values reported in the literature were achieved. Hence, results indicate that porosity defects have significant influence on the mechanical properties and repeatability of as-printed samples. By minimizing these defects via the proposed printability framework, high ductility and strength of binary NiNb₅ alloy were achieved. Furthermore, this framework enables determining processing windows for newly developed AM alloys in an efficient and accelerated fashion and using readily available resources for AM practitioners without relying on proprietary models and codes.

References

A. S. for Testing (2009), “M. C. B. on metal powders, M. P. Products, standard test methods for density of compacted or sintered powder metallurgy (PM) Products using Archimedes’ principle”, *ASTM International*.

Ar Isoy, Y.M., Criales, L.E., Özel, T., Lane, B., Moylan, S. and Donmez, A. (2017), “Influence of scan strategy and process parameters on microstructure and its optimization in additively manufactured nickel alloy 625 via laser powder

bed fusion”, *The International Journal of Advanced Manufacturing Technology*, Vol. 90 Nos 5/8, pp. 1393-1417.

Atli, K., Boon, H., Seede, R., Zhang, B., Elwany, A., Arroyave, R. and Karaman, I. (2021), “Laser-based additive manufacturing of a binary ni-5wt.%nb alloy”, *Journal of Manufacturing Processes*, Vol. 62, pp. 720-728.

Boley, C., Mitchell, S., Rubenchik, A. and Wu, S. (2016), “Metal powder absorptivity: modeling and experiment”, *Applied Optics*, Vol. 55 No. 23, pp. 6496-6500.

Bosio, F., Aversa, A., Lorusso, M., Marola, S., Gianoglio, D., Battezzati, L., Fino, P., Manfredi, D. and Lombardi, M. (2019), “A time-saving and cost-effective method to process alloys by laser powder bed fusion”, *Materials & Design*, Vol. 181, p. 107949.

Brandt, M. (2016), *Laser Additive Manufacturing: Materials, Design, Technologies, and Applications*, Woodhead Publishing.

Campbell, K. (2006), “Statistical calibration of computer simulations”, *Reliability Engineering & System Safety*, Vol. 91 Nos 10/11, pp. 1358-1363.

Chase, M. Jr, (1996), Nist-janaf thermochemical tables fourth edition, J. Phys. Chem. Ref. Data, Monograph 9.

Cotteleer, M. and Joyce, J. (2014), “3d opportunity: additive manufacturing paths to performance, innovation, and growth”, *Deloitte Review*, Vol. 14, pp. 5-19.

Eagar, T.W. and Tsai, N.S. (1983), “Temperature fields produced by traveling distributed heat sources”, *Welding Journal*, Vol. 62 No. 12, pp. 346-355.

Fayazfar, H., Salarian, M., Rogalsky, A., Sarker, D., Russo, P., Paserin, V. and Toyserkani, E. (2018), “A critical review of powder-based additive manufacturing of ferrous alloys: process parameters, microstructure and mechanical properties”, *Materials & Design*, Vol. 144, pp. 98-128.

Hanzl, P., Zetek, M., Bakša, T. and Kroupa, T. (2015), “The influence of processing parameters on the mechanical properties of slm parts”, *Procedia Engineering*, Vol. 100 No. 1, pp. 1405-1413.

Hu, Z. and Mahadevan, S. (2017), “Uncertainty quantification in prediction of material properties during additive manufacturing”, *Scripta Materialia*, Vol. 135, pp. 135-140.

ImageJ, R.W. (2012), “Us natl institutes heal bethesda”, maryland, usa, available at: imagej.nih.gov/ij

Johnson, L., Mahmoudi, M., Zhang, B., Seede, R., Huang, X., Maier, J.T., Maier, H.J., Karaman, I., Elwany, A. and Arróyave, R. (2019), “Assessing printability maps in additive manufacturing of metal alloys”, *Acta Materialia*, Vol. 176, pp. 199-210.

Karayagiz, K., Johnson, L., Seede, R., Attari, V., Zhang, B., Huang, X., Ghosh, S., Duong, T., Karaman, I., Elwany, A. and Arróyave, R. (2020), “Finite interface dissipation phase field modeling of ni–nb under additive manufacturing conditions”, *Acta Materialia*, Vol. 185, pp. 320-339.

Kasperovich, G., Haubrich, J., Gussone, J. and Requena, G. (2016), “Correlation between porosity and processing parameters in tial6v4 produced by selective laser melting”, *Materials & Design*, Vol. 105, pp. 160-170.

Kennedy, M.C. and O’Hagan, A. (2001), “Bayesian calibration of computer models”, *Journal of the Royal Statistical Society: Series B (Statistical Methodology)*, Vol. 63 No. 3, pp. 425-464.

- King, W.E., Barth, H.D., Castillo, V.M., Gallegos, G.F., Gibbs, J.W., Hahn, D.E., Kamath, C. and Rubenchik, A.M. (2014), "Observation of keyhole-mode laser melting in laser powder-bed fusion additive manufacturing", *Journal of Materials Processing Technology*, Vol. 214 No. 12, pp. 2915-2925.
- Krol, T., Seidel, C. and Zaeh, M. (2013), "Prioritization of process parameters for an efficient optimisation of additive manufacturing by means of a finite element method", *Procedia Cirp*, Vol. 12, pp. 169-174.
- Letenneur, M., Kreitchberg, A. and Brailovski, V. (2019), "Optimization of laser powder bed fusion processing using a combination of melt Pool modeling and design of experiment approaches: density control", *Journal of Manufacturing and Materials Processing*, Vol. 3 No. 1, p. 21.
- Mahmoudi, M., Tapia, G., Karayagiz, K., Franco, B., Ma, J., Arroyave, R., Karaman, I. and Elwany, A. (2018), "Multivariate calibration and experimental validation of a 3d finite element thermal model for laser powder bed fusion metal additive manufacturing", *Integrating Materials and Manufacturing Innovation*, Vol. 7 No. 3, pp. 116-135.
- Mingear, J., Zhang, B., Hartl, D. and Elwany, A. (2019), "Effect of process parameters and electropolishing on the surface roughness of interior channels in additively manufactured nickel-titanium shape memory alloy actuators", *Additive Manufacturing*, Vol. 27, pp. 565-575.
- Ngo, T.D., Kashani, A., Imbalzano, G., Nguyen, K.T. and Hui, D. (2018), "Additive manufacturing (3d printing): a review of materials, methods, applications and challenges", *Composites Part B: Engineering*, Vol. 143, pp. 172-196.
- Schoinochoritis, B., Chantzis, D. and Salonitis, K. (2017), "Simulation of metallic powder bed additive manufacturing processes with the finite element method: a critical review", *Proceedings of the Institution of Mechanical Engineers, Part B: Journal of Engineering Manufacture*, Vol. 231 No. 1, pp. 96-117.
- Seede, R., Shoukr, D., Zhang, B., Whitt, A., Gibbons, S., Flater, P., Elwany, A., Arroyave, R. and Karaman, I. (2020),

- "An ultra-high strength martensitic steel fabricated using selective laser melting additive manufacturing: densification, microstructure, and mechanical properties", *Acta Materialia*, Vol. 186, pp. 199-214.
- Song, B., Dong, S., Zhang, B., Liao, H. and Coddet, C. (2012), "Effects of processing parameters on microstructure and mechanical property of selective laser melted ti6al4v", *Materials & Design*, Vol. 35, pp. 120-125.
- Spierings, A.B., Schneider, M. and Eggenberger, R. (2011), *Comparison of Density Measurement Techniques for Additive Manufactured Metallic Parts*, Rapid Prototyping Journal.
- Valencia, J.J. and Quested, P.N. (2013), Thermophysical properties.
- Wang, Z., Liu, P., Xiao, Y., Cui, X., Hu, Z. and Chen, L. (2019), "A data-driven approach for process optimization of metallic additive manufacturing under uncertainty", *Journal of Manufacturing Science and Engineering*, Vol. 141 No. 8.
- Yadroitsev, I., Krakhmalev, P., Yadroitsava, I., Johansson, S. and Smurov, I. (2013), "Energy input effect on morphology and microstructure of selective laser melting single track from metallic powder", *Journal of Materials Processing Technology*, Vol. 213 No. 4, pp. 606-613.
- Yap, C.Y., Tan, H.K., Du, Z., Chua, C.K. and Dong, Z. (2021), *Selective Laser Melting of Nickel Powder*, Rapid Prototyping Journal.
- Zhang, Y., Evans, J.R. and Yang, S. (2011), "Corrected values for boiling points and enthalpies of vaporization of elements in handbooks", *Journal of Chemical & Engineering Data*, Vol. 56 No. 2, pp. 328-337.
- Zhou, X., Liu, X., Zhang, D., Shen, Z. and Liu, W. (2015), "Balling phenomena in selective laser melted tungsten", *Journal of Materials Processing Technology*, Vol. 222, pp. 33-42.

Corresponding author

Alaa Elwany can be contacted at: elwany@tamu.edu